Smet Sarah (Orcid ID: 0000-0001-5011-184X)

Characterization by X-ray µCT of the air-filled porosity of an agricultural soil at different matric potentials

Sarah Smet[a1*], Erwan Plougonven[b], Angélique Léonard[b], and Aurore Degré[a]

[a] Soil Water Plant Exchanges, TERRA Teaching and Research Center, Gembloux Agro-Bio Tech, University of Liège, Gembloux, Belgium
[b] Chemical Engineering, University of Liège, Liège, Belgium

Contact information
Dr. Sarah Smet, sarah.smet@gmail.com. Orcid: 0000-0001-5011-184X
Dr. Plougonven, eplougonven@uliege.be. Orcid : 0000-0003-2935-8121
Prof. Léonard, a.leonard@uliege.be. Orcid: 0000-0001-7287-4936
Prof. Degré, aurore.degre@uliege.be. Orcid: 0000-0001-6912-6136
*Corresponding author: Sarah Smet (sarah.smet@gmail.com)

Running title
Characterization of a draining soil with X-ray CT

Keywords
3D computed tomography, Capillary theory, Connectivity, Tortuosity, Soil pore space, Soil water retention curve

Highlights

- Visualization of the same soil samples at various water matric potentials with X-ray µCT
- Quantitative confirmation that capillary theory does not accurately predict the pore size distribution
- The geometrictortuosity of the air-filled soil pore network decreases in X-ray µCT image acquired at lower matric potential
- The air-filled pore space of the soil and its connectivity mostly increase with decreasing matric potential

[1] Currently affiliated to Department of Geography, University of Namur, Namur, Belgium.

This article has been accepted for publication and undergone full peer review but has not been through the copyediting, typesetting, pagination and proofreading process which may lead to differences between this version and the Version of Record. Please cite this article as doi: 10.1111/ejss.13387

Abstract

To describe various important soil processes like the release of greenhouse gases or the proliferation of microorganisms, it is necessary to assess quantitatively how the geometry and in particular the connectivity of the air-filled pore space of a soil evolves as it is progressively dried. The availability of X-ray computed microtomography (μCT) images of soil samples now allows this information to be obtained directly, without having to rely on the interpretation of macroscopic measurements using capillary theory, as used to be the case. In this general context, we present different methods to describe quantitatively the configuration of the air-filled pore space in 3D μCT images of 20 separate samples of a loamy soil equilibrated at different matric potentials. Even though measures using μCT on such multi-scale materials strongly depends on image resolution, our results show that in general, soil samples most often behave as expected, e.g., connectivity increases with higher negative matric potential, while tortuosity decreases. However, simple correlations could not be found between the evolution of quantitative descriptors of the pore space at the different matric potentials and routinely measured macroscopic soil parameters. A statistical analysis of all soil samples concurrently confirmed this lack of correspondence.

1. Introduction

In the 1930s and 40s, soil physicists like Haines (1930) and Childs (1940) argued that the size distribution of soil particles, routinely measured since the 18th century (Baveye, 2013) and still used extensively to this date to map soils, provided very little useful information concerning the retention of water and its transport in soils. This realization led to a shift of emphasis from soil particles to the "water-occupied void space [...,] which largely determines the gross physical properties of soils" (Childs and Collis-George, 1948).

These authors suggested that soil voids, or "pores", could be linked to straight capillaries of varying diameters, and that their size distribution would provide the type of direct quantitative information needed to describe the functioning of soils. This perspective has since been adopted in most soil physics textbooks to explain the principles that govern the retention of water in soils and its movement, and led to the development in the 1960s and 1970s, of various computer modelling techniques to describe these processes, assimilating soil pores to networks of straight, cylindrical capillaries (e.g., Thullner and Baveye, 2008; Raoof and Hassanizadeh, 2010). As a result, a significant body of research has relied on measurements of the pore size distribution (PSD) of soils to predict a wide range of processes of interest, such as gas diffusion, water retention and flow, mechanical resistance, carbon dynamics, microbial colonization, and root penetration, as well as to assess the effect of different management practices and degradation processes on soil productivity. In recent years, several authors have suggested that the fate of soil organic matter, and in particular its mineralization, could be described accurately using models that rely on a simple partitioning of the pore space into distinct pore size classes, regardless of their spatial distribution relative to each other (e.g., Kuka et al., 2007; Waring et al., 2020).

Early on, however, researchers realized that the measurement of the pore size distribution of very heterogeneous materials such as soils was fraught with difficulties, manifested among other things by the routinely observed influence of sample size (e.g., Simms and Yanful, 2002; Tao et al., 2019). The root cause of these difficulties was ascribed to the fact that pores of different sizes were necessarily connected to each other and influenced each other's individual behaviours in ways that did not necessarily correspond to what capillarity theory predicts in terms of a normal response to conditions imposed on the outer surfaces of soil samples. It was suspected that large pores connected to the outside surface of soil samples only through much smaller pores should not be expected at all to empty or fill according to capillarity theory. This phenomenon, generally referred to as the ink-bottle effect (e.g., Moro and Böhni, 2002), has long been considered to account for the hysteresis that affects the water retention in soils. Over the last two decades, the increasingly widespread availability of table-top X-ray computed microtomography (X-ray μCT) scanners has allowed researchers to obtain direct visual confirmation that the connectivity of the pore space in soils is indeed crucial to a full understanding of soil processes.

Over the last 2 decades, a significant body of literature has dealt with the use of X-ray μCT to quantify the connectivity and tortuosity of the pore space in soil samples that were dried prior to scanning. Comparatively little work has been carried out on wet or partially wet samples. On one hand, several studies investigated the fate of the soil structure when submitted to one (Bottinelli et al., 2016; Mady et al., 2020; Fomin et al., 2023) or several wetting-drying cycles

(Diel et al., 2019; Pires et al., 2020). On the other hand, Pot et al. (2015) scanned soil samples at different moisture contents, to obtain data with which to compare computer simulations of the spatial distribution of moisture in the pore space. Rabot et al. (2015) performed similar measurements to understand how the moisture-dependent connectivity of the air-filled pore space affected the observed sudden flushing out of N_2O upon desaturation of soil samples. In neither one of these two papers, nor in any one of a handful of more recent articles that have also looked at wet soil samples, have the geometrical characteristics of the evolving air-filled porosity in progressively drying soil samples been quantified in parallel to the hydrodynamic properties of the samples. Such insight is direly needed to be able to predict processes like the release of greenhouse gases (Blagodatsky and Smith, 2012) or the proliferation of fungal hyphae (Soufan et al., 2018), among others. Intuitively, one would venture the qualitative guess that the tortuosity and connectivity of the air-filled pore space in a given soil sample should decrease and increase, respectively, when the matric potential decreases (i.e., the air-filled porosity increases), but any attempt to model microscale processes in soils requires the respective trends to be precisely quantified numerically.

In that general context, the primary objective of this research is to assess quantitatively how the geometry and in particular the connectivity of the air-filled pore space of a soil evolves as it is progressively dried. The analysis is based on X-ray μCT images of soil samples obtained after the samples were equilibrated at successively decreasing matric potentials, and different mathematical techniques, including fractal geometry, were used to describe the pore space. In the results section, after a short discussion of the influence of image resolution on the computation of the parameters of interest, we review how some of the targeted quantitative measures vary in individual soil samples with decreasing matric potential. Finally we present the outcome of a statistical analysis of all soil samples concurrently, to find out to what extent trends manifested by individual samples hold more generally in the agricultural fields where samples were obtained.

2. Materials and methods

2.1. Soil description and sampling

The studied soil is a typical loamy soil from the intensive agricultural area of Gembloux, Belgium, composed on average of 14.3 % of clay, 78.3% of silt and 7.4% of sand. Twenty samples were collected from an agricultural field and 48h after the last rain event with plastic cylinders (3 cm in diameter x 5 cm in height) driven manually into the soil until the top of the cylinder was at the surface level and then manually excavated. Ten samples were collected in the summer of 2015, ten others in the summer of 2016. Each year, half of the samples were collected from a "reduced tillage" experimental site at which minimal field work was carried out, including stubble breaking before sowing. The other half of the samples was obtained at the site of a "conventional tillage experiment", seven months after ploughing at 25 cm depth. The tillage experiment was conducted by Hiel et al. (2018). We collected samples from fields having experienced distinct agricultural practices in order to visualize differences in the geometry of the pore networks, as well as a variation in laboratory-measured physical soil properties.

2.2 Laboratory measurements

With the understanding that each soil sample presents a unique pore space architecture and therefore a distinct pore space configuration, we measured the hydraulic properties of each soil sample individually. To measure the soil water retention curve (SWRC) using a pressure plate apparatus (Richards, 1948 and DIN ISO 11274, 2012), the soil samples were first slowly upward-saturated with distilled water. After equilibration at several steps of the SWRC (-1, -4, -7, -10, -30 and -70 kPa water potential), the air permeability k_a was measured with an Eijkelkamp air permeameter 08.65 (Eijkelkamp Agrisearch Equipment, Giesbeek, The Netherlands). This equipment applies a constant air flow through the sample, and the resulting inlet pressure is measured. At the end of the SWRC measurements, the soil samples were again saturated and their saturated hydraulic conductivity (Ks [LT^{-1}]) was measured using a constant head device (Rowell, 1991) and applying Darcy's law. Finally, the soil samples were oven-dried at 105° for seven days to obtain their dry weight. Porosity [L^3L^{-3}] was calculated as the ratio between the volume of water within the saturated soil sample and its total volume (McKenzie et al., 2002).

2.3 X-ray micro-computed tomography

At most of the equilibration steps mentioned above in the measurements of the SWRC, the soil samples were scanned, again individually, using a Skyscan-1172 desktop micro-CT system (Brüker microCT, Kontich, Belgium). The X-ray source was set at 100kV and 100µA and an aluminum-copper filter was used to minimize the beam hardening. The rotation step was set at 0.3° over 180° and an averaging of 2 projections was recorded at each rotation step. 4 x 4 binning was used, and pixel size was set at 21.5 µm. This gives a field of view of 21 x 14 mm, so to cover the entire sample, a 2x4 grid of sub-regions was scanned. Finally, exposure time for each projection was 600 ms, making a total acquisition of approximately 4 hours. Acquisition parameters remained the same for all soil samples and all water potentials, to avoid any influence on geometry characterization (e.g., Peng et al., 2014; Shah et al., 2016). Likewise, parameters for the tomographic reconstruction and image processing were identical, unless specified otherwise. Reconstruction was performed with the NRecon® (v. 1.6.3.3) software, freely provided by Brüker with an automatic misalignment compensation and a ring artefact correction (level 7). No beam hardening correction was applied during the reconstruction because the correction parameters is user-dependent and can have a profound unquantified effects on the resulting images. After reconstructions, the 3D images were cropped to select only the volume within the sampling cylinders (radius of 700 pixels) and the image contrast was improved in Matlab (MathWorks, UK) using the "imadjust" function.

2.3 Image processing

Prior to segmentation, a 3D median filter with a radius of 2 pixels was applied to the images to decrease noise (Smet et al., 2018a) and increase segmentation quality. A 2x2x2 sub-sampling to reduce computational cost increased the pixel size from 21.5 µm to 43 µm. As suggested by Houston et al. (2013) and Shah et al. (2016), it is advisable to acquire images of soil samples at the smallest voxel size possible even if a post-scan coarsening is necessary for practical reasons. Nevertheless, a comparison was carried out of the same 3D image processed at 21.5 µm and 43 µm resolutions for one of the soil samples to determine the extent to which image resolution

affected the analysis. We applied a 3D median filter with a radius of 4 pixels to a copy of the stack of images of one sample (#12) in order to analyze it at a resolution of 21.5 µm.

We applied a global segmentation method (Otsu, 1979; Beckers et al., 2014a.) to convert each individual grayscale image into a binary image where the void phase (air-filled pore space) and the other phases (including the water-filled pore space and soil particles) are differentiated through the definition of a unique threshold. The threshold was defined at the onset with Otsu's method (1979) in ImageJ (Schneider et al., 2012), then adjusted through an iterative loop to minimize the difference between the air-filled porosity (µCT_PO) of the soil sample visible in the image and the laboratory-measured porosity of the soil sample at a water potential of - 1 kPa. This segmentation method has been proven satisfactory and robust (Beckers et al., 2014b, Smet et al., 2018b). This crucial segmentation step impacts the subsequent description of the air-filled pore space (Smet al., 2018a; Beckers et al., 2014a; Lamandé et al., 2013; Peth et al., 2008; Peng et al., 2014; Tarquis et al., 2009), and visual inspection was performed before any further analysis of the binary images. All scanning parameters were kept constant between each image acquisition of one soil sample at several water potentials. However, since the water content of the sample influences the resulting histogram, we therefore defined the threshold independently for each 3D image.

The binary images were processed both in Avizo, with a code developed by Plougonven (2009), and in Image J (Schneider et al., 2012) with the BoneJ plugin (Doube et al., 2010). Air-filled pores of minimum 5 voxels were considered in the analysis and we calculated parameters that are commonly used to define the pore space configuration, in particular the Euler number (ε, -), the geometric tortuosity (τ, -) and the fractal dimension (FD, -) for each 3D image. The fractal dimension was calculated with a box-counting algorithm (Perret et al., 2003). The geometric tortuosity (τ) between two points is the ratio between the effective pore path and the shortest distance between the two extreme points (Perret et al., 1999). The global tortuosity is obtained by computing the average of the tortuosities associated with each of the branches (continuous line of connected voxels). The Euler number is a quantification of the connectivity. Following Vogel et al. (2010), it is calculated with the formula $\varepsilon = N-L+O$, where N denotes the number of isolated objects; L is the number of redundant connections and O represents the number of cavities or holes (Vogel et al., 2010). The more negative the Euler number is, the more connected the medium. In Avizo, the pores are quantified based on the definition of a pore as "part of the pore space, homotopic to a ball, bounded by the solid, and connected to other pores by throats of minimal surface area" (Plougonven, 2009). Pore boundaries are demarcated by the local geometry. The resulting 3D quantification information regarding pore chambers connected by pore throats includes pore localization, volumes, specific surface, connected surfaces, number of connections, and inertia tensors. From those data, we calculated the visible porosity (µCT_PO, -), the average coordination number (Avg_Z, -), the average surface connectivity (SC, -) and the global connectivity (Γ, -). We explored several definitions of the connectivity as each parameter conveys complementary information about the complexity of the soil pore space geometry (Lucas et al., 2021). Avg_Z is the average number of connections at one point (Perret et al., 1999) whereas SC is an average of the normalized connected surfaces of pores (number of connections multiplied by connection area, divided by the pore volume). Finally, the global connectivity (Renard et Allard, 2013) measures the probability that two separate pore voxels are part of the connected component.

2.5 Statistical analyses

To determine if the evolutions of structural parameters with decreasing matric potential, observed in individual samples, translate to a general trend across all of them, different statistical analyses were carried out. First, for each global parameters, a randomized complete block design was used toconduct a two-wat analysis of variance (ANOVA), followed by a post-hoc Tukey test if the results were significant. Afterwards, a two-way analysis of covariance (ANCOVA) was carried out using the laboratory soil measurements (K_s, k_a) as covariates. The efficiency of the ANCOVA over the ANOVA (ratio of residual squared means) was calculated in cases where the addition of a covariate would adjust the means and return a non-significant difference between images at various water potentials.

Afterwards, a principal component analysis was performed to identify similarities between individuals (one individual being one 3D image) as well as a K-clustering analysis to quantitatively validate the spatial results obtained from the PCA. The package FactoMineR (Lê et al., 2008) was used in R.

3. Results

3.1 Influence of image resolution

As stated previously, to facilitate the treatment of typically voluminous X-ray CT images and the subsequent computation of microscale parameters, the resolution of the images has been systematically coarsened from 21.5 µm to 43 µm. Several authors in the past have pointed out that a change in resolution unavoidably affects the outcome of any quantitative image analysis, for a number of different reasons (e.g., Houston et al., 2013; Peng et al., 2014; Shah et al., 2016). Since we carried out identical analyses on the nonsubsampled image associated with one randomly selected sample (#12, equilibrated at a matric potential of -70 kPa), we can estimate the extent of this resolution effect.

Visual inspection of a cross-section in the original and coarsened images, along with their segmented counterparts to highlight the differences (Figure 1), indicates that there are differences between the original, grayscale images, and that these differences become even more apparent in the binary images, obtained after segmentation. These slight differences translate into distinct values of a number of parameters computed from the images (Table 1). Some of the changes with resolution are not entirely intuitive. In particular, the image at the lowest resolution (43 µm) exhibits a larger porosity than the one at the highest resolution (21.5 µm). The difference is small, and it is clear that in the loamy soil that was sampled, much of the finer porosity cannot be seen by the CT scanner even at the highest resolution. Still, the fact that the porosity is highest in the lowest-resolution image probably results from the noise reduction steps during the image manipulation, as well as the segmentation itself, where smallest pores have probably been excluded.

3.2 Quantitative assessment of structural parameters of individual soil samples

In principle, one expects that as the matric potential decreases, the air-filled porosity µCT_PO and the pore connectivity should increase, whereas the pore network tortuosity should decrease. This is indeed generally what we observe but sometimes unexpected patterns emerge. For example, µCT_PO increase with water potential for most samples, but remain almost

constant for a few or negligibly decreased for one sample: sample #9 has a µCT_PO that varies from 6.67 % to 6.43% (Table 2). In these cases, the visible macroporosity was probably already drained at low water potential. Mady et al., (2020) also observed increasing µCT_PO when scanning soil samples at increasing negative potentials (-5 kPa, -15 kPa and -50 kPa). Their scanning resolution was 10.5 µm and this implies that all visible pore space should already be drained at -5 kPa, as per capillary theory. They however attributed this µCT_PO change to, among other structural reasons, the replacement of water by air in the pore space.

More µCT_PO implies more pores and more connecting paths, with means less tortuosity, which is what we observe for our samples shown in Figure 2 and Figure 3. Globally, the average coordination number (Avg_Z, Figure 4) increase with decreasing water potential, as does the global connectivity (Γ, Figure 5). Both are related to the porosity. The higher the porosity, the larger the probability Γ that two pore voxels belong to the same pore and the more connections there are per pore, Avg_Z. It is more erratic for the surface connectivity (SC, Figure 6) and the Euler number (ε, Figure 7). When pores become visible with the decreasing water potential, these are not necessarily connected to the rest of the pore network with visible pores, increasing the number of isolated objects that influence both ε and SC.

It would be very useful in practice, for modeling purposes, to be able to predict the evolution of the tortuosity and connectivity of a pore network a priori on the basis of routinely laboratory-measured soil physical properties. The various measurements we carried out enable us to monitor the evolution of Γ and τ with, e.g., the laboratory-measured air-filled porosity (Figure 8). We drew trendlines and we highlight the power-shape relationship between air-filled porosity and τ, which has been observed by Zhang et al. (2020) who worked at lower scale (aggregate) and higher resolution (1.5 µm). However, probably due to the fact that each soil sample has such a unique pore space configuration, attempts we made to use measured values of Ks, ka, or parameters associated with a mathematical description of the SWRC failed to predict the observed evolution of the connectivity or tortuosity.

3.3 Statistical analysis of parameter values for all soil samples

The analysis in the previous section shows that it is possible to evaluate quantitatively the influence of the desaturation of each soil sample on a number of structural parameters that should be useful to model a range of microscale processes occurring in soils. Since, as was shown as well, different soil samples behave sometimes very differently with respect to individual parameters, one might be interested to know to what extent definite trends emerge for the whole population of 20 samples, overall.

One way to find out is to plot average parameter values as a function of the matric potential, and their associated standard deviation, as in Figure 9 for the tortuosity and for the global connectivity. This type of graphic provides visual information about the average values that are significantly different from others, at different matric potential. Several box-plots with parameters variations between the lowest matric potential (-4 kPa) and the other matric potentials (-7, -10, -30 and -70 kPa) confirm the individual trends (Fig. 10) with a slightly decreasing τ, an increasing pore network connectivity (through Avg_Z and Γ) with higher negative matric potentials. Quantifying the pore space structure of repacked soil samples scanned at a resolution of 8 µm and at various moisture states (-2.5 kPa and approximately -100 kPa), Diel et al. (2019) observed that Γ would decrease with a decreasing µCT_PO but non

linearly as µCT_PO can be dominated by one connected cluster at higher µCT_PO while it breaks up into isolated pore clusters at lower µCT_PO. Decreasing τ with increasing µCT_PO has already been observed (e.g. Katuwal et al. 2015) and Sandin et al. (2017) reported positive correlation between µCT_PO and Γ with a working resolution close to ours. The ε variations are less convincing. A more negative ε translates a higher pore network connectivity through a higher number of redundant connections but ε value will be largely influenced by the number of unconnected pores/cluster, by the number of smaller pores. Within the frame of this study, an increasing µCT_PO do not therefore necessarily lead to an increased ε, as the newly visible porosity is no necessarily connected to the visible pore network through visible connections. Lucas et al (2021) evaluated the pore network connectivity as function of scale and resolution and also pointed that ε would increase towards positive values with the emergence of smaller pores that are likely not connected to the next smaller pore size class. Katuwal et al. (2015) found significant positive correlations between visible macroporosity (images with a resolution of 430 µm) and ε and suggested that ε was not an appropriate metric to study their samples as those were characterized with isolated macropores. Recently, Fomin et al. (2023) observed increasing ε values, not necessarily significantly different, when scanning undisturbed soil samples at saturation and at matric potential of +/- 0.25; 3 and 10 kPa with a voxel size of 7.91 µm.

Beside evaluating trends, a more rigorous approach consists of carrying out a full-fledged analysis of variance, as in Table 3. The statistical analysis confirms that the µCT_PO globally increase between almost all combinations of waterpotentials, from lower to higher negative water potentials. Difference between -30 kPa and -70 kPa is not significant, and the same situation pertains for other parameters. As expected, the fractal dimension significantly increase between several water potentials. Indeed, positive correlations between µCT_PO and FD have often been observed in the literature (Rachman et al., 2005; Larbso et al., 2014, Smet et al., 2018b). The connectivity indicators are significantly different when the differences in water potentials are larger. No differences are significant between -4 and -7 or -10 kPa, or between -7 and -10 kPa (except for Avg_Z), although the µCT_PO are increasing. This is in agreement with the sample SWRC where the drop in water content occurs between -10 and -70 kPa (Figure 11), suggesting that the released water is contained in a few macropores rather than in a multitude of narrower (and invisible) pores. The SWRC in this figure is typical for this type of soil and representative of all samples. Interestingly, when adding, to the ANOVA, covariates representing the soil static and dynamic physical properties, the test is not significant anymore for a few parameters, as shown in Table 4. Statistically, this corresponds to cases where the difference between two means is significant because of the covariate. Under the conditions of this study, the differences in µCT_PO between two water potentials are significant because of the intrinsic hydrodynamic properties of the soil sample, $\log(K_s)$. It is likewise for FD, the Euler number and Avg_Z. The global connectivity evolution between water matricpotentials is related to the soil air permeability, k_a. The tortuosity, although being significantly different between -4 kPa and any other water potentials, is not linked to any static or dynamic soil physical properties, neither is SC.

A principal component analysis (PCA) was conducted where the 100 PCA individuals were the 20 samples acquired at five matric potentials, and the variables were the microscopic structural parameters It reveals that although presenting varying global parameters with water

potentials, the combination of all the parameters of the samples remains similar between water potentials, in other words, the coordinates of the first four dimensions of the PCA remain similar between water potentials for each sample (Fig. 12 for the first and second dimensions). We quantitatively confirm this with a K-clustering analysis showing that, for most samples, the images acquired at various water potentials belong to the same cluster, except for the images acquired at -4 kPa. The differences in parameters were indeed mostly between -4 kPa and any other water potentials (Table 5). We therefore observed significant intra-samples difference between water potential through the ANOVA analysis, but more difference between samples which suggest that the evolution of the parameters of each sample is restricted, because of the uniqueness of the pore configuration of each sample.

4. Discussion

As per capillary theory, soil pores of +/- 33 µm in radius should be drained at a matric potential of -4kPa, but it is without considering the soil pore space geometry. Hunt et al. (2013) named the part of porosity that cannot drained because of unusable pathways, *the inaccessible porosity*. Knowing that the pore connectivity plays an essential role in water retention, our initial assumption was that visualizing soil at a water matric potential of -4 kPa or -70 kPa, and steps in between, would lead to different microscopic characteristics of the air-filled pore space measured on X-ray images with a 43 µm resolution. Prior to the analyses of the images, we aimed to evaluate the potentialities of using X-ray images with a 21.5 resolution to visualize more small pores that would drain between -4 and -70 kPa. Because it would have been too computationally demanding to carry out all the image processing and parameter calculation steps with the images at the 21.5 µm resolution, the rest of the analysis was performed with the lower resolution images instead. It is crucial to remember in that context that the parameter values obtained in the course of this analysis are necessarily resolution-dependent, and are not absolute. More generally, as pointed out earlier by Baveye et al. (2010) and Houston et al. (2017), one should keep in mind that these values depend on the many different steps taken during the acquisition of the images as well as during their processing. A potential complement of this study would be to process the images with their original resolution. Pot et al. (2020) recently again showed that image-calculated hydraulic conductivity can changed by up to two orders of magnitude when changing the image resolution, image depth, noise reduction or segmentation method.

The analysis conducted by individual samples confirmed that the characteristics of a draining pore space, derived from X-ray CT images, are varying due to an increasing visible air-filled porosity and confirming that the capillary theory, as valuable as it may be to introduce concepts in soil physics, does not account for the crucial importance of the connectivity of pores. Pot et al. (2015) had also concluded that applying strictly the capillary theory to morphological pore scale model failed to replicate experimental observations.

The relationships between the increasing µCT_PO, due to the increasing negative matric potential, and the X-ray-derived microscopic parameters are in line with existing literature but we would like to point out the current trend of studying the soil pore network by pore classes and pore types rather than through global metrics (e.g. Lucas et al., 2020).

To understand the mechanisms of the bio-chemical soil processes, it is essential to study individual soil samples, but a global statistical analysis was performed to confirm the

differences of microscopic parameters values between the X-ray images acquired at different matric potentials. Through the ANCOVA analysis, it is spotlighted again that the differences in pore space at various matric potentials are linked to the intrinsic soil properties such as hydraulic conductivity and air permeability. It has indeed been already observed that the pore space connectivity affects the air permeability (Paradelo et al., 2016) and saturated hydraulic conductivity (Sandin et al., 2017; Smet et al., 2018b). We here again confirm the importance of the soil pore space geometry on the soil properties (Rabot et al., 2018).

5. Conclusion

Over the last few years, the crucial practical importance of the release of greenhouse gases by soils or the maintenance of soil biodiversity under changing environmental conditions has heightened interest in the quantitative description of how the air-filled pore space in soils changes when soils progressively desaturate, i.e., when their matric potential becomes increasingly negative. The increasing availability of X-ray tomography scanners all around the world enables this type of question to be addressed directly in undisturbed soil samples. However, up to now, very few measurements have been carried out in partially saturated soil samples, and no attempt has been made to quantify the evolution of the geometrical features of the visible air-filled pore space as the soil dries. In this context, one of the key results of the research presented in this article is to show that this quantification, which is unavoidably relative to the resolution of the µCT images, is definitely feasible. Our results show that most soil samples, among the 20 that were part of the study, behave according to expectations, in the sense that, e.g., their connectivity increases and their tortuosity decreases as the matric potential is lowered. However, a few soil samples exhibit different patterns, which we discuss in detail, and hypothesize to be due to the various treatment steps used in the treatment of the images. We attempted to come up with simple quantitative relationships between descriptors of the spatial configuration of the pore space and macroscopic parameters, like the hydraulic conductivity K_s, the air permeability k_a, or parameters associated with a mathematical description of the soil water retention curve SWRC, which are all routinely measured in the laboratory. However, our attempts failed to identify clear relationships. In the case of the SWRC, this emphasizes the fact that the description of the SWRC using capillary theory, as used to be traditional before the advent of computed tomography scanners, is fundamentally inadequate, since that theory does not account for the connectivity of the air-filled pore space, which clearly evolves over time when a soil dries. A statistical analysis of all soil samples concurrently, motivated by the fact that soil samples tended to behave very differently from each other and by the desire to find out how things could be described at spatial scales larger than just that of individual soil samples, confirmed the lack of correspondence between descriptors of the evolving air-filled pore space and routinely measured macroscopic soil parameters. Hopefully, the data gathered during the course of this research will be useful in the future to elaborate new theories describing quantitatively how the geometry of the air-filled pore space evolves as soils dry, and will lead to better models of the functions of soils under changing environmental conditions.

Data availability

The data and images generated during the course of this research are fully available from the lead author upon request.

Funding statement

This work was funded through a Ph.D. grant awarded to SS (FRIA, FNRS, Brussels, Belgium) and a FNRS grand awarded to EP (R.FNRS.3363-T.1094.4)

Acknowledgement

The authors acknowledge the support of the National Fund for Scientific Research (Brussels, Belgium). SS would like to particularly thank Prof. P. C. Baveye for the recent highly constructive discussions. The anonymous reviewers and the Associate Editors are also thanked for their constructive comments.

Conflict of interest disclosure

The authors declare that they have no conflict of interest regarding the research described in this article.

References

Baveye, P.C., 2013. Jean-Baptiste De Beunie (1717–1793): unsung pioneer of the study of soils. Soil Sci. 178 (2), 55–59.

Beckers, E., Plougonven, E., Gigot, N., Léonard, A., Roisin, C., Brostaux, Y. et al., 2014a. Coupling X-ray microtomography and macroscopic soil measurements: a method to enhance near saturation functions ? Hydrol. Earth Syst. Sci. 18, 1805-1817.

Beckers, E., Plougonven, E., Roisin, C., Hapca, S., Léonard, A., and Degré, A., 2014b. X-ray microtomography: A porosity-based thresholding method to improve soil pore network characteristization? Geoderma. 219-220, 145-154.

Blagodatsky, S., Smith, P., 2012. Soil physics meets soil biology: towards better mechanistic prediction of greenhouse gas emissions from soil. Soil Biology and Biochemistry, *47*, 78-92.

Bottinelli, N., Zhou, H., Boivin, P., Zhang, Z.B., Jouquet, P., Hartmann, C. and Peng, X. 2016. Macropores generated during shrinkage in two paddy soils using X-ray micro-computed tomography. Geoderma. 78-86.

Childs, E.C., 1940. The use of soil moisture characteristics in soil studies. Soil Sci. 50 (1), 239–252.

Childs, E.C., Collis-George, N.C., 1948. Soil geometry and soil-water equilibria. Trans. Faraday Soc. 44 (3), 78–85.

Diel, J., Vogel, H.-J. and Schlüter, S. 2019. Impact of wetting and drying cycles on soil structure dynamics. Geoderma. 63-71.

Doube, M., Klosowski, M. M., and Arganda-Carreras, I. et al., 2010. Bone-J: Free and extensible bone image analysis in ImageJ. Bone. 47(6), 1076-1079.

Fomin, D., Yudina, A.V., Romanenko, K.A., Abrosimov, K.N., Karsanina, M.V. and Gerke, K.M. 2023. Soil pore structure dynamics under steady-state wetting-drying cycle. Geoderma. 116401.

Haines, W.B., 1930. Studies in the physical properties of soils. The hysteresis effect in capillary properties, and the modes of moisture distribution associated herewith. J. Agric. Sci. 20, 97–116.

Hiel, M. P., Barbieux, S., Pierreux, J., Olivier, C., Lobet, G., Roisin, C., Garré, S., Colinet, G., Bodson, B., and Dumont, B., 2018. Impact of crop residue management on crop production and soil chemistry after seven years of crop rotation in temperate climate, loamy soils. PeerJ. 6, e4836. doi: https://doi.org/10.7717/peerj.4836.

Houston, A. N., Schmidt, S., Tarquis, A. M., Otten, W., Baveye, P. C., Hapca, S. M., 2013. Effect of scanning and image reconstruction settings in X-ray computed microtomography on quality and segmentation of 3D soil images. Geoderma, *207*, 154-165.

Houston, A. N., Otten, W., Falconer, R., Monga, O., Baveye, P. C., Hapca, S. M., 2017. Quantification of the pore size distribution of soils: assessment of existing software using tomographic and synthetic 3D images. Geoderma, *299*, 73-82.

Hunt, A. G., Ewing, R. P., and Horton, R. 2013. What's wrong with soil physics? Soil Sci. Soc. Am. J. 77, 1877-1887. Doi: 10.2136/sssaj2013.01.0020

Katuwal, S., Norgaard, T., Moldrup, P., Lamandé, M., Wildenschild, D., and de Jonge, L. W. 2015. Linking air and water transport in intact soils to macropore characteristics inferred from X-ray computed tomography. Geoderma. 237-238, 9-20.

Kuka, K., Franko, U., Ruhlmann, J., 2007. Modelling the impact of pore space distribution on carbon turnover. Ecological Modelling, 208, 295–306. https://doi.org/10.1016/j.ecolmodel.2007.06.002.

Lamandé, M., Wildenschild, D., Berisso, F.E., Garbout, A., Marsh, M., Moldrup, P., et al., 2013. X-ray CT and laboratory measurements on glacial till subsoil cores: assessment of inherent and compaction-affected soil structure characteristics. Soil Sci. 178(7), 359-368.

Lê, S., Josse, J., Husson, F.2008. FactoMineR: A Package for Multivariate Analysis. Journal of Statistical Software*,* 25(1), 1–18. doi:10.18637/jss.v025.i01

Lucas, M., Vetterlein, D., Vogel, H-J., Schlüter, S. 2021. Revealing pore connectivity across scales and resolutions with X-ray CT. Eur. J. Soil. Sci. 72, 546-560.

Mady, A. and Shein, E.V. 2020. Assessment of pore space changes during drying and wetting cycles in hysteresis of soil water retention curve in Russia using X-ray computed tomography. Geoderma Regional. e00259.

McKenzie, N., Coughlan, K., and Cresswell, H., 2002. Soil physical measurement and interpretation for land evaluation. Collingwood, Australia: Csiro Publishing.

Moro, F., Böhni, H., 2002. Ink-bottle effect in mercury intrusion porosimetry of cement-based materials. Journal of Colloid and Interface Science, 246(1), 135–149. https://doi.org/10.1006/jcis.2001.7962.

Otsu, N., 1979. A threshold selection method from gray-level histograms. IEEE Trans. Syst. Man Cybern. 9, 62-66.

Paradelo, M., Katuwal, S., Moldrup, P., Norgaard, T., Herath, L., and de Jonge, L. W. (2016). X-ray CT-derived characteristics explain varying air, water, and solute transport properties across a loamy field. Vadose Zone J. 192, 194–202. doi: 10.2136/vzj2015.07.0104

Peng, S., Marone, F., Dultz, S., 2014. Resolution effect in X-ray microcomputed tomography imaging and small pore's contribution to permeability for a Berea sandstone. Journal of Hydrology, 510, 403-411.

Perret, J. S., Prasher, S. O., Kantzas, A., and Langford, C., 1999. Three- dimensional quantification of macropore networks in undisturbed Soil Cores. Soil Sci. Soc. Am. J. 63, 1530-1543. doi:10.2136/sssaj1999.6361530x

Perret, J. S., Prasher, S. O., and Kacimov, A. R., 2003. Mass fractal dimension of soil macropores using computed tomography: from the box-counting to the cube-counting algorithm. Eur. J. Soil Sci. 54, 569-579.

Peth, S., Horn, R., Beckmann, F., Donath, T. Fischer, J., and Smucker, A. J. M., 2008. Three-dimensional quantification of intra-aggregate pore-space features using synchrotron-radiation-based microtomography. Soil Sci. Soc. Am. J. 72(4), 897-908.

Pires, L.F., Auler, A.C., Roque, W.L. and Mooney, S.J. 2020. X-ray microtomography analysis of soil pore structure dynamics under wetting and drying cycles. Geoderma. 114103.

Plougonven, E., 2009. Link between the microstructure of porous materials and their permeability. [PhD thesis]. [Bordeaux, France]: Université Sciences et Technologies - Bordeaux I.

Pot, V., Peth, S., Monga, O., Vogel, L. E., Genty, A., Garnier, P., et al., 2015. Three-dimensional distribution of water and air in soil pores: comparison of two-phase two-relaxation-times lattice-Boltzmann and morphological model outputs with synchrotron X-ray computed tomography data. Adv. in Water Resources, 84, 87-102.

Pot, V., Zhong, X., and Baveye, P. C. 2020. Effect of resolution, reconstruction settings, and segmentation methods on the numerical calculation of saturated soil hydraulic conductivity from 3D computed tomography images. Geoderma. 362, 114089.

Raoof, A., Hassanizadeh, S. M., 2010. A new method for generating pore-network models of porous media. Transport in porous media, 81(3), 391-407.

Rabot, E., Lacoste, M., Hénault, C., Cousin, I., 2015. Using X-ray co mputed tomography to describe the dynamics of nitrous oxide emissions during soil drying. Vadose Zone Journal, 14(8), 1-10.

Rachman, A., Anderson, S. H., and Gantzer, C. J., 2005. Computed-Tomographic measurements of soil microporosity parameters as affected by stiff-stemmed grass hedges. Soil Sci. Soc. Am. J. 69, 1609-1616. doi: 10.2136/sssaj2004.0312

Renard, P., and Allard, D. (2013). Connectivity metrics for subsurface flow and transport. Adv. Wat. Res. 51, 168-196. doi: 10.1016/j.advwatres.2011.12.001.

Richards, L.A., 1948. Porous plate apparatus for measuring moisture retention and transmission by soils. Soil Sci. 66, 105-110.

Rowell, D. L., 1994. Soil Science: methods and application. Department of Soil Science, University of Reading : Longman Scientific & Technical.

Sandin, M., Koestel, J., Jarvis, N., and Larsbo, M., 2017. Post-tillage evolution of structural pore space and saturated and near-saturated hydraulic conductivity in a clay loam soil. Soil Til. Res. 165, 161–168. doi: 10.1016/j.still.2016.08.004

Schneider, C.A., Rasband, W. S., and Eliceiri, K. W., 2012. NIH Image to ImageJ: 25 years of image analysis. Nature methods. 9(7), 671-675.

Simms, P. H., Yanful, E. K. (2002). Predicting soil—water characteristic curves of compacted plastic soils from measured pore-size distributions. Géotechnique, 52(4), 269-278.

Shah, S. M., Gray, F., Crawshaw, J. P., Boek, E. S., 2016. Micro-computed tomography pore-scale study of flow in porous media: Effect of voxel resolution. Advances in water resources, *95*, 276-287.

Smet, S., Plougonven, E., Léonard, A., Degré, A., and Beckers, E., 2018a. X-ray Micro-CT: how soil pore space description can be altered by image processing. Vadose Zone J. 17:160049. doi: 10.3389/fenvs.2018.00020

Smet, S., Plougonven, E., Léonard, A., Degré, A., and Beckers, E., 2018b. Can the pore scale geometry explain soil sample scale hydrodynamic properties?. Front. Environ. Sci. 6:20. doi: 10.2136/vzj2016.06.0049.

Soufan, R., Delaunay, Y., Gonod, L. V., Shor, L. M., Garnier, P., Otten, W., Baveye, P. C., 2018. Pore-scale monitoring of the effect of microarchitecture on fungal growth in a two-dimensional soil-like micromodel. Frontiers in Environmental Science, *6*, 68.

Tao, G., Chen, Y., Xiao, H., Chen, Q., Wan, J., 2019. Determining soil-water characteristic curves from mercury intrusion porosimeter test data using fractal theory. Energies, *12*(4), 752.

Tarquis, A. M., Heck, R. J., Andina, D., Alvarez, A., and Antón, J. M., 2009. Pore network complexity and thresholding of 3D soil images. Ecol. Complex. 6, 230-239.

Thullner, M., Baveye, P., 2008. Computational pore network modeling of the influence of biofilm permeability on bioclogging in porous media. Biotechnology and Bioengineering, *99*(6), 1337-1351.

Vogel, H-J., Weller, U., and Schlüter, S., 2010. Quantification of soil structure based on Minkowski functions. Comput. Geosci. 36, 1236-1245.

Waring, B. G., Sulman, B. N., Reed, S., Peyton Smith, A., Averill, C., Creamer, C. A., Cusack, D. F., Hall, S. J., Jastrow, J. D., Jilling, A., Kemner, K. M., Kleber, M., Liu, X.-J. A., Pett-Ridge, J., Schulz, M., 2020. From pools to flow: The PROMISE framework for new insights on soil carbon cycling in a changing world. Global Change Biology, 26, 6631–6643. https://doi.org/10.1111/gcb.15365.

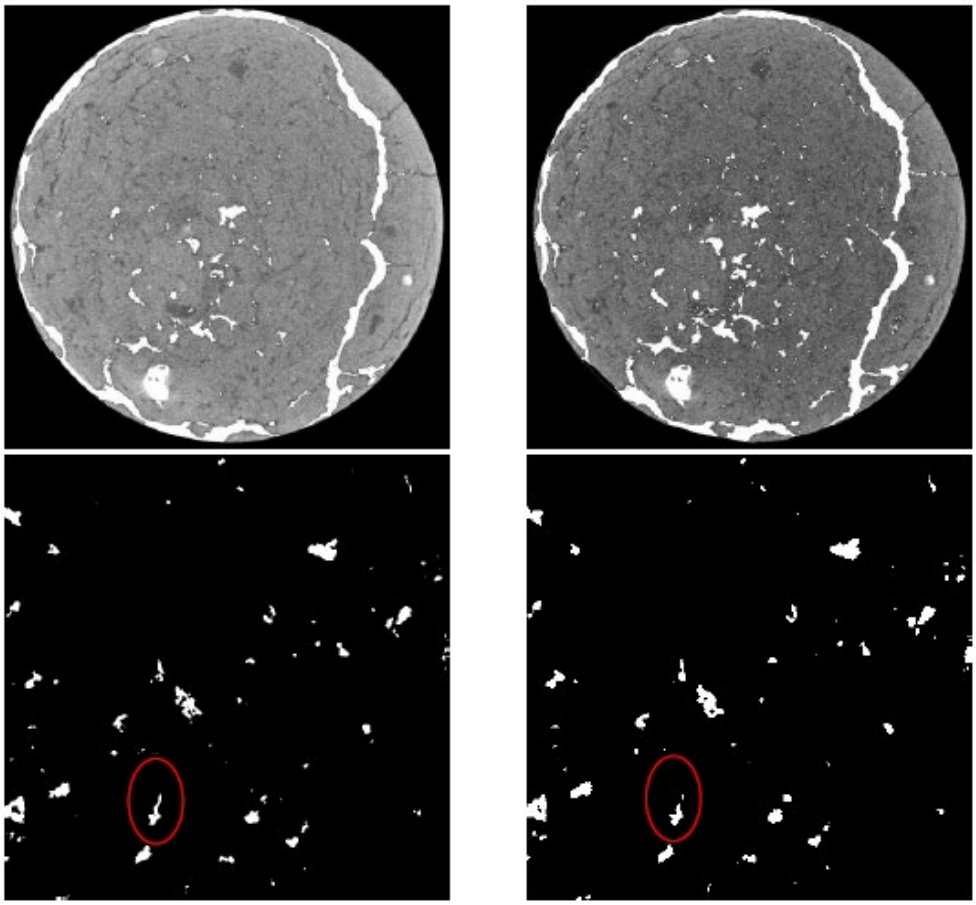

Figure 1. X-ray CT images illustrating the influence of the resolution for one of the samples (#12). Images on the left are at the original resolution of 21.5 µm. whereas those on the right are at the coarsened (resampled) resolution of 43 µm, eventually used for the bulk of the analyses. Upper row: grayscale images with the pores highlighted in white. Lower row: Zoomed viewed of an identical portion of the associated binary images, after thresholding. In the area encircled in red, a single pore in the highest resolution image (left) has become divided into two apparently separate ones in the image on the right.

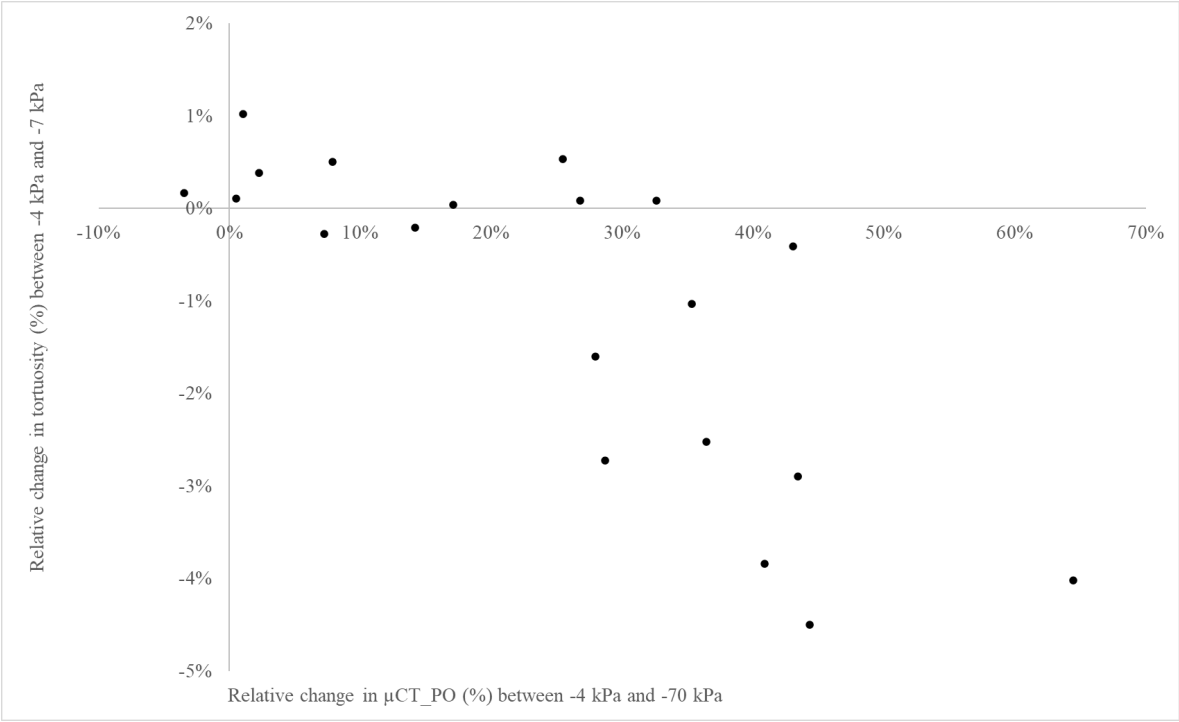

Figure 2. Relative change in visible air-filled porosity from the X-ray CT images (µCT_PO) between water potential of -4 kPa to -70 kPa versus the relative change in tortuosity (τ) between water potential of -4 kPa to -70 kPa.

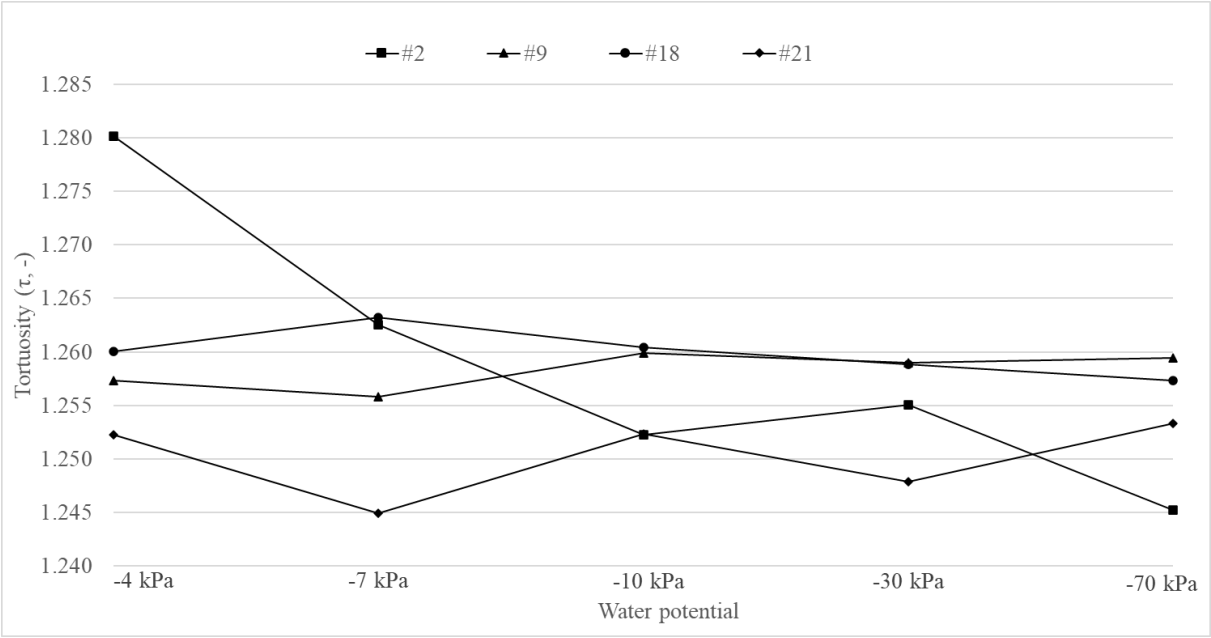

Figure 3. Evolution of the pore network tortuosity (τ) with water potential (kPa) for four samples.

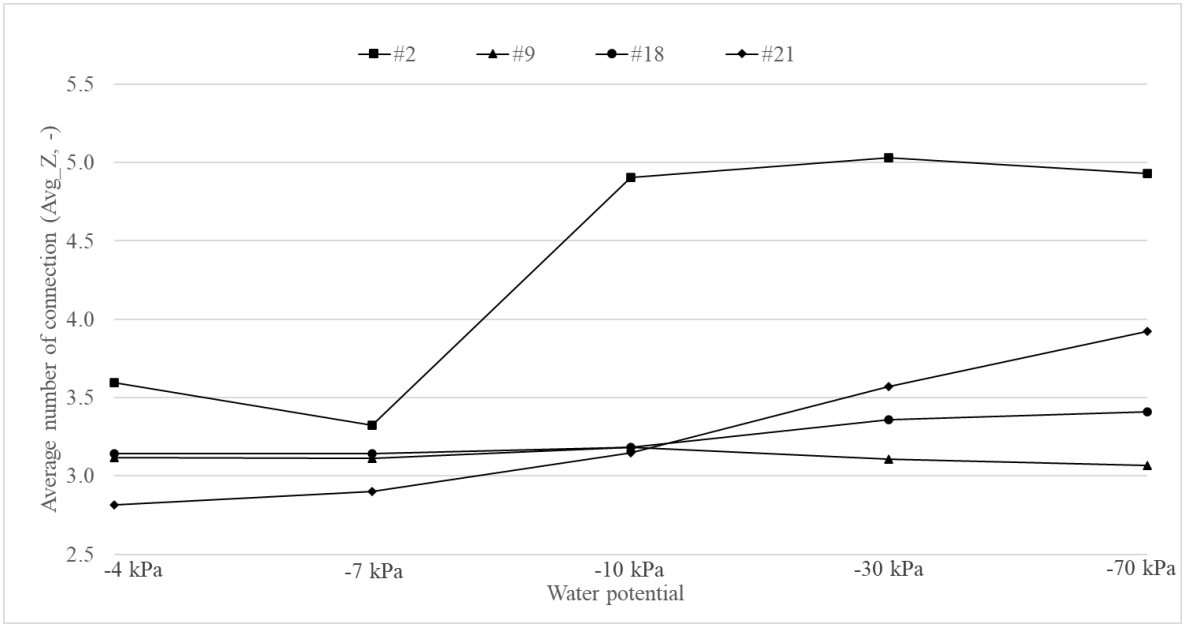

Figure 4. Evolution of the average number of coordination (Avg_Z) with water potential (kPa) for four samples.

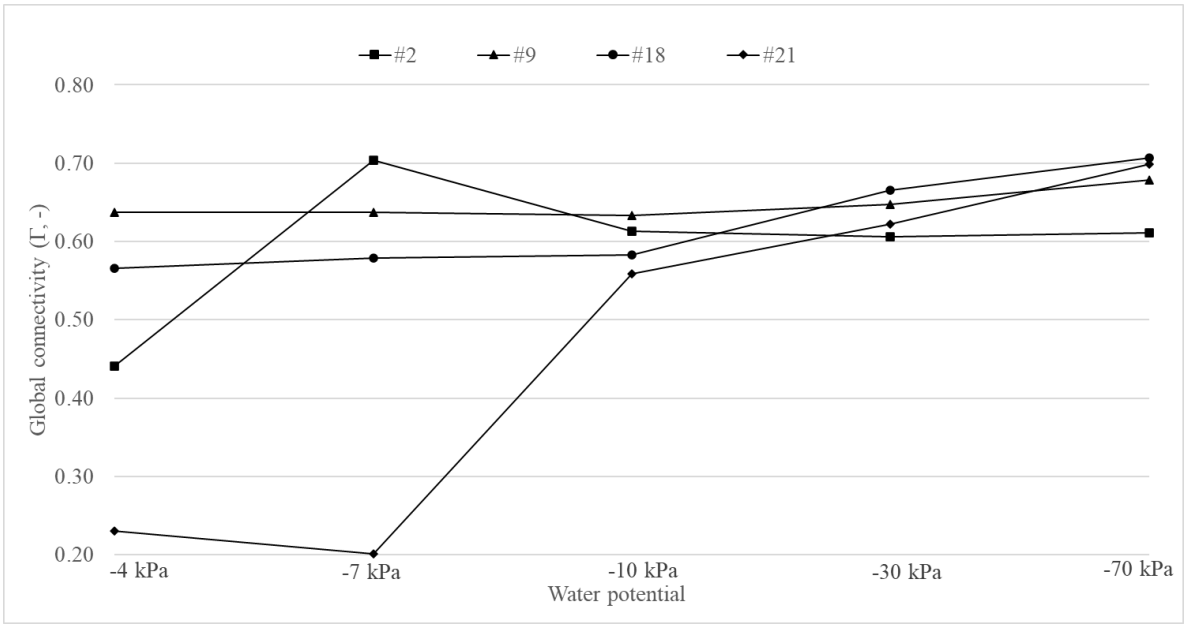

Figure 5. Evolution of the global connectivity (Γ) with water potential (kPa) for four samples.

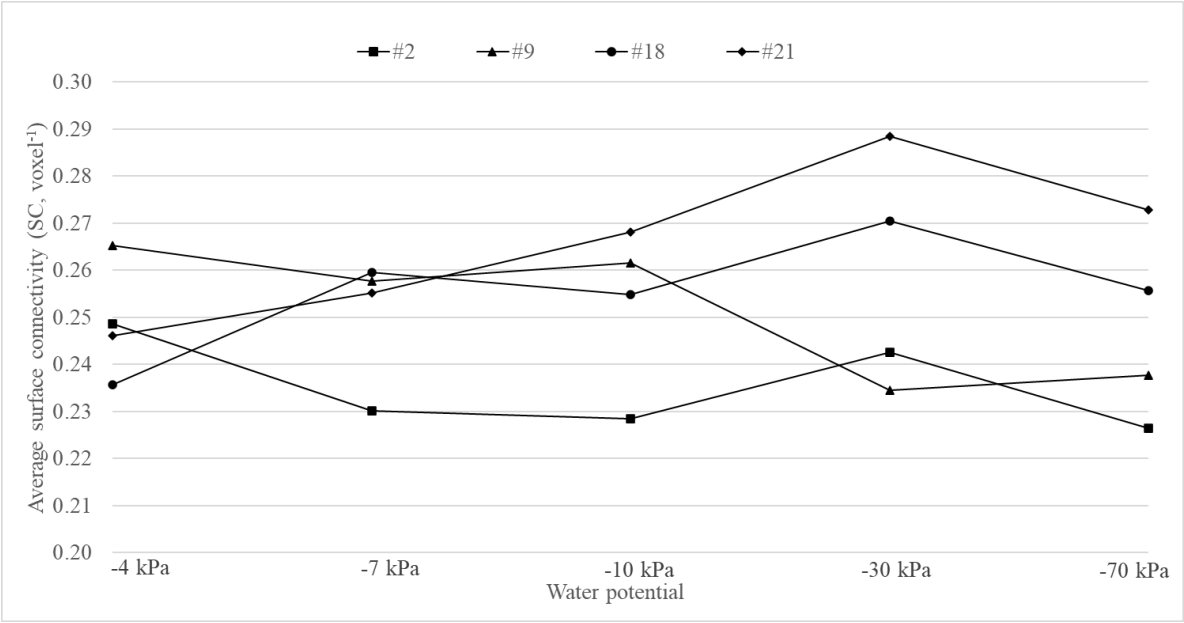

Figure 6. Evolution of the averaged surface connectivity (SC) with water potential (kPa) for four samples.

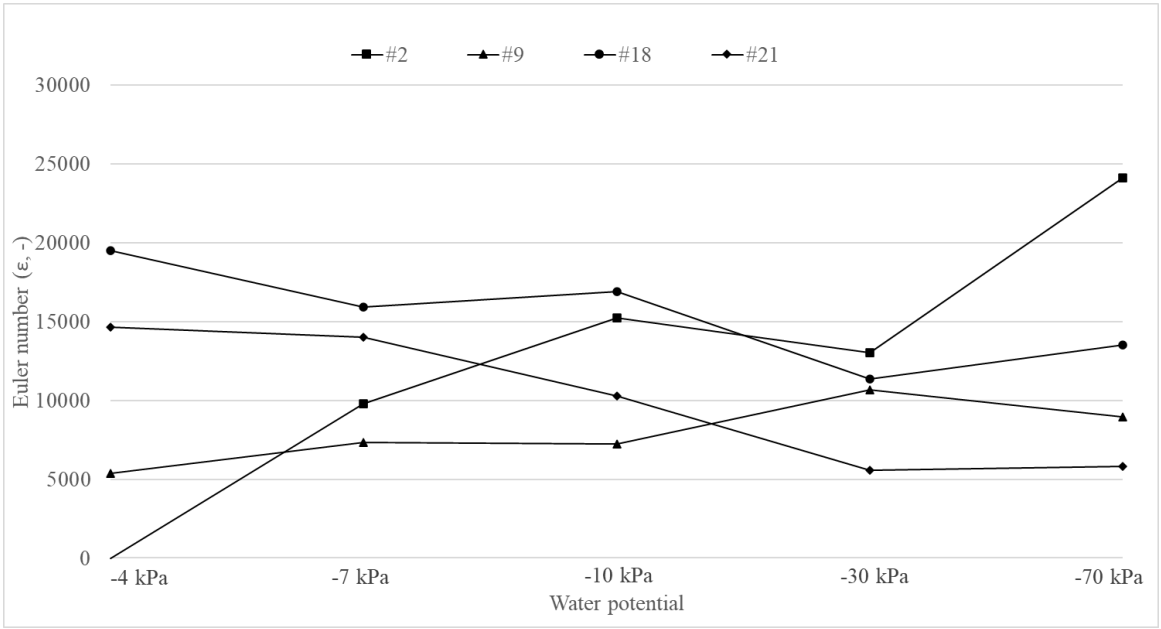

Figure 7. Evolution of the Euler number (ε) with water potential (kPa) for four samples.

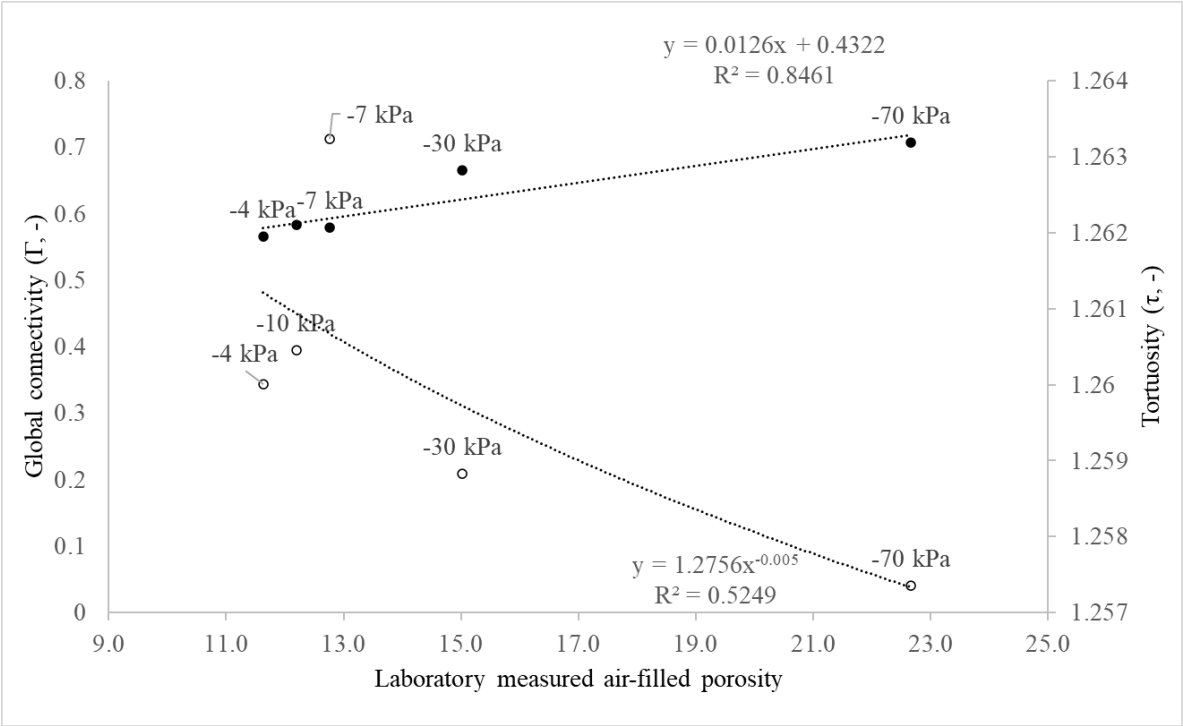

Figure 8. Evolution of the laboratory-measured air-filled porosity with water potential (kPa) versus the evolution of the global connectivity (black dots) and tortuosity (white dots) with water potential (kPa) for all samples.

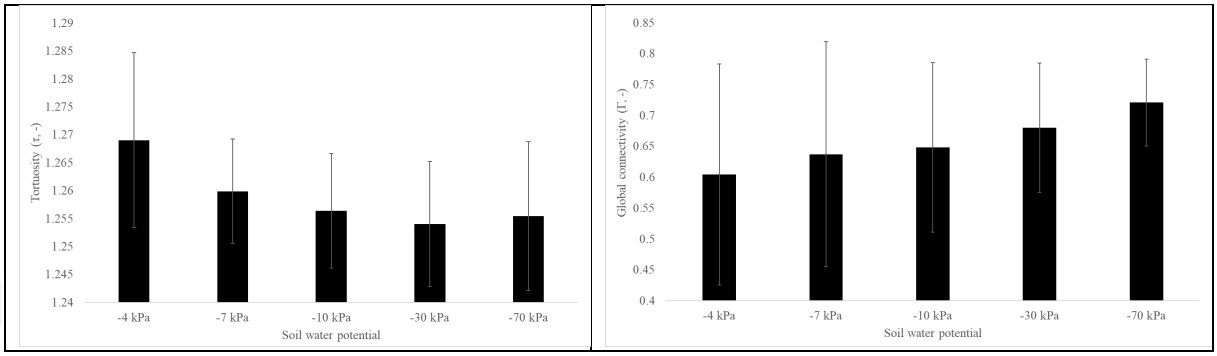

Figure 9. Average tortuosity (τ) and average global connectivity (Γ), and their respective standard deviation of all soil samples for all water potentials.

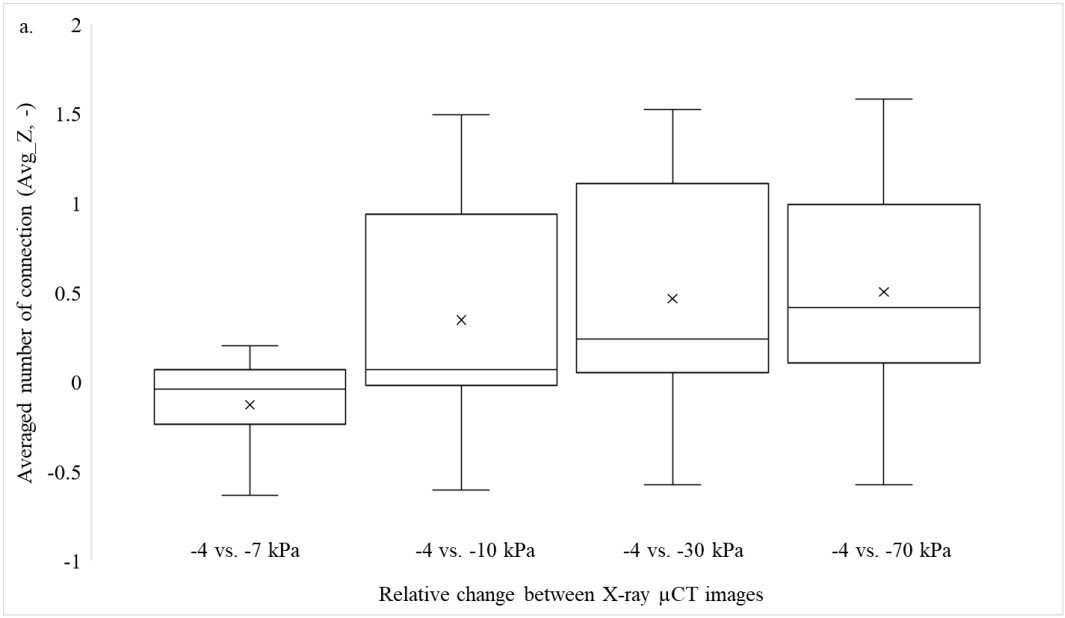

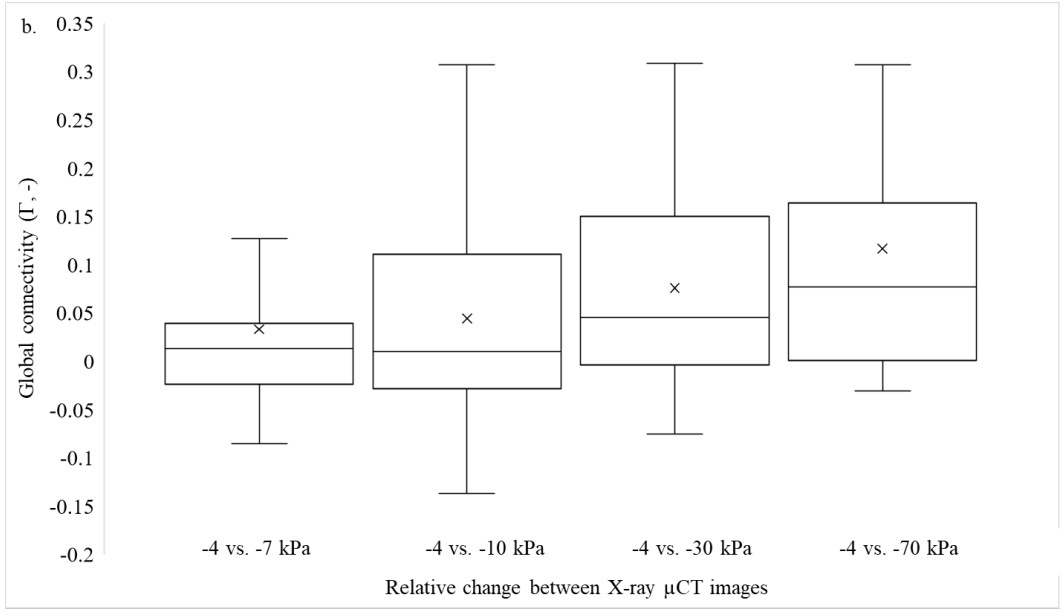

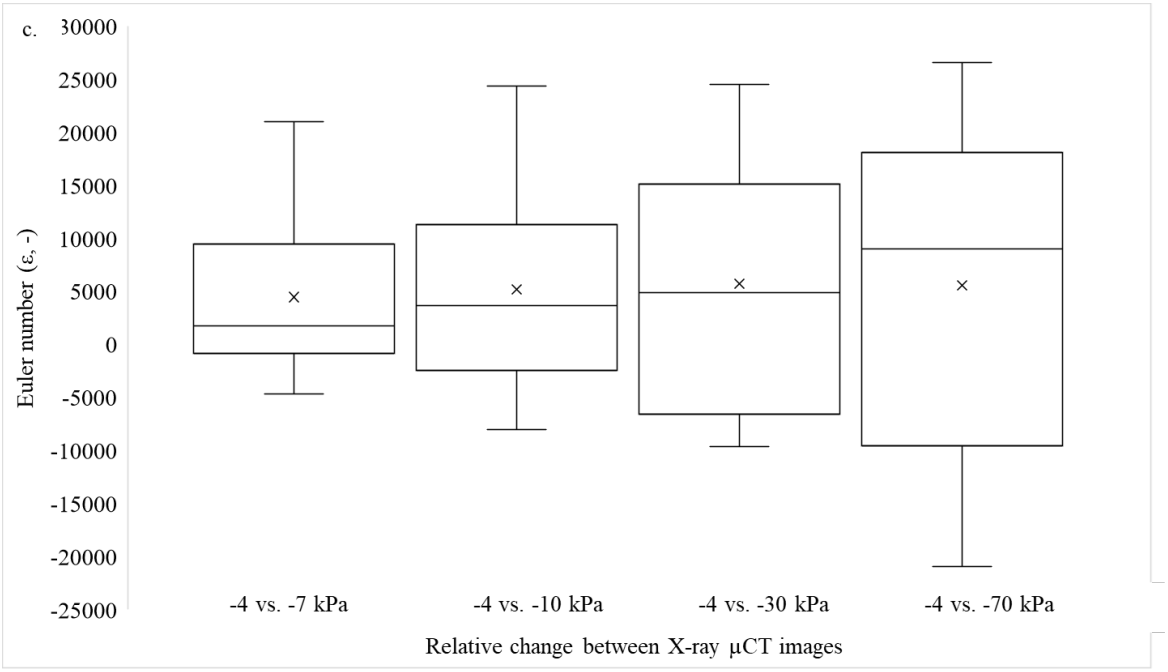

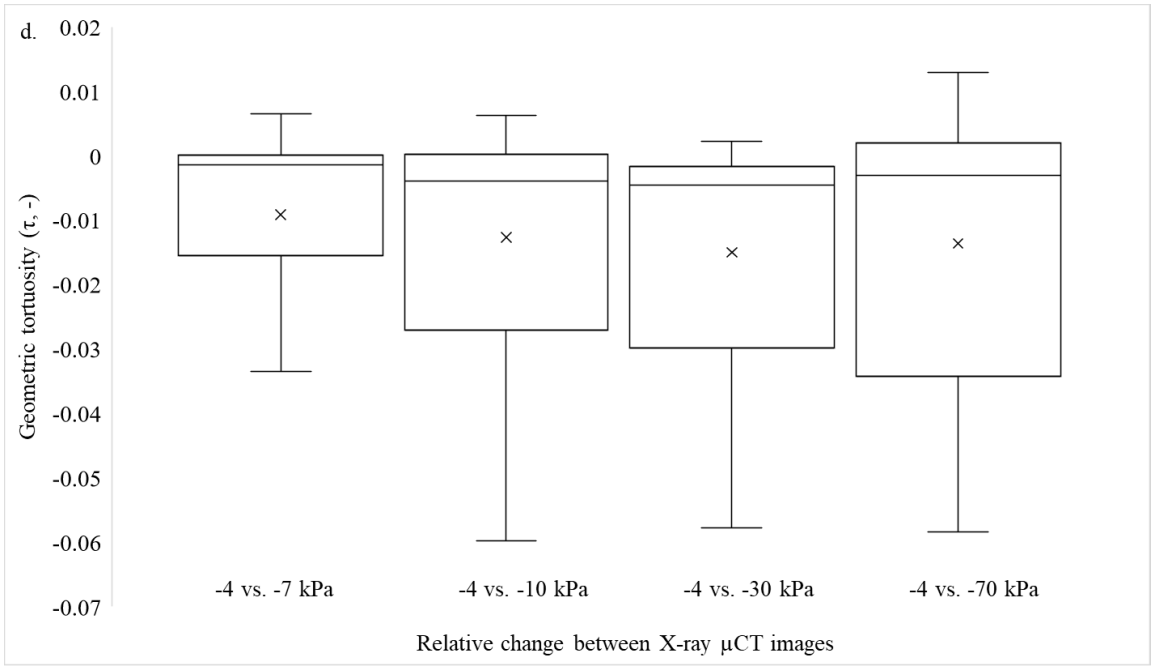

Figure 10. Relative change in microscopic parameters between images acquired at -4 kPa and at -7, -10, -30 and -70 kPa. a. Averaged number of connection, b. Global connectivity (Γ), c Euler number (ε), and d. tortuosity (τ). The boxplots present the first and third quartile, the median (line), the mean (cross) and extremes values.

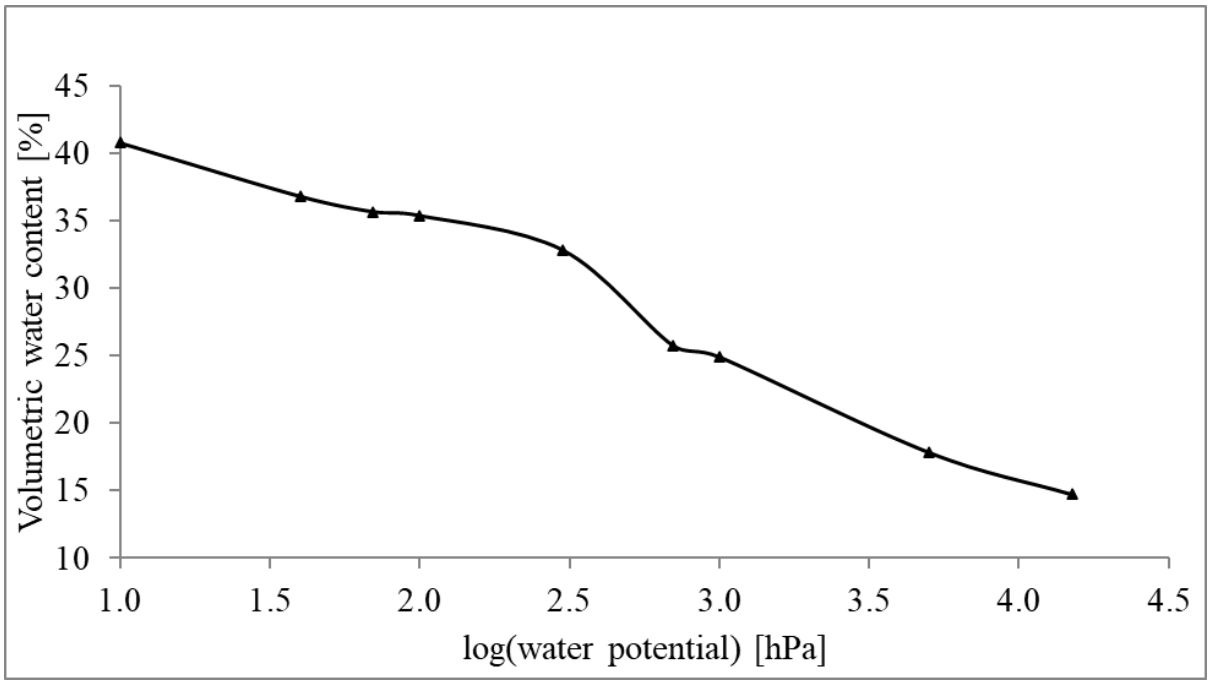

Figure 11. Soil water retention curve of the sample #14.

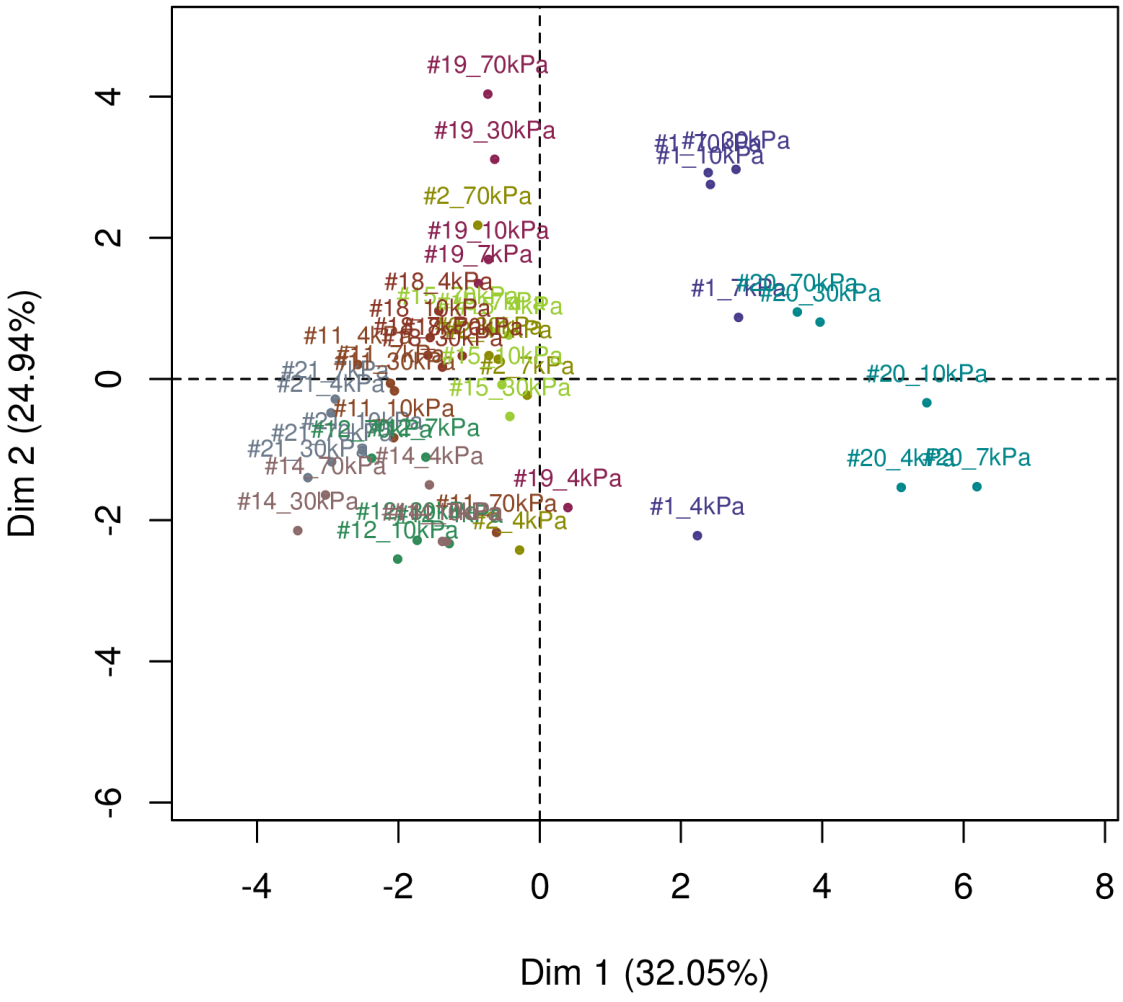

Figure 12. First and second dimension of the PCA. Each color represents one soil samples at various matric potentials.

Table 1. Porosity and connectivity parameters (the visible air-filled porosity. µCT_PO; the averaged volume of the pore. Avg_Vol; the fractal dimension. FD; the average number of coordination. Avg_Z; the surface connectivity. SC; the global connectivity. Γ; the tortuosity. τ; the Euler number. ε) associated with sample #12 in the case of the X-ray CT images at 21.5 and 43 µm resolutions.

Parameter	Resolution	
	21.5 µm	43 µm
µCT_PO [%]	5.410	7.207
Avg_Vol [mm3]	3.70E-02	4.42E-02
FD [-]	2.366	2.554
Avg_Z [-]	5.607	3.742
SC [voxel-1]	0.209	0.283
Γ [-]	0.998	0.714
ε [-]	6018	7226
τ [-]	1.253	1.280

Table 2. Visible air-filled porosity from the X-ray CT images (µCT_PO) for each sample at -70 kPa water potential and their relative change rate (%) in µCT_PO between a water potential of -4 kPa to -70 kPa.

Sample	µCT_PO at -70kPa (%)	Relative change between -4 kPa and -70 kPa (%)
#1	14.23	30.71
#2	6.63	22.31
#3	12.91	29.01
#4	9.31	26.72
#5	9.25	21.13
#6	6.23	30.27
#7	7.50	6.77
#8	7.01	26.10
#9	6.43	-3.57
#11	3.71	7.29
#12	7.21	1.03
#14	5.09	20.30
#15	8.51	14.60
#18	6.05	12.44
#19	12.20	39.19
#20	9.50	21.85

#21	4.56	24.60
#22	9.52	0.49
#23	2.76	30.09
#24	12.77	2.21

Table 3. Results of the two-way ANOVA comparing the average value of the descriptive parameters of the pore space configuration (the visible air-filled porosity. µCT_PO; the Euler number. ε; the fractal dimension. FD; the tortuosity. τ; the average number of coordination. Avg_Z; the surface connectivity. SC; the global connectivity. Γ) at various water potential**s.**

	comparison between scans at water matric potential [kPa] of									
	4-7	4-10	4-30	4-70	7-10	7-30	7-70	10-30	10-70	30-70
µCT_PO	*	*	*	*			*	*	*	
ε			*	*						
FD		*	*	*			*			
τ	*	*	*	*						
AvgZ			*	*	*	*	*			
SC										
Γ			*	*			*		*	

Table 4. Relative efficiency of the ANCOVA over the ANOVA performed on the X-ray CT parameters (the visible air-filled porosity. µCT_PO; the Euler number. ε; the fractal dimension. FD; the tortuosity. τ; the average number of coordination. Avg_Z; the surface connectivity. SC; the global connectivity. Γ) with associate covariate (hydraulic conductivity at saturation (Ks). air permeability (ka). The relative efficiency is the ratio of residual squared mean of ANOVA without and with covariate.

Covariates	**µCT_PO**	**ε**	**FD**	**τ**	**Avg_Z**	**SC**	**IPO**	**Γ**
log(Ks)	17.08	1.92	5.41		4.20		4.86	
log(ka)		1.92	0.83					0.96

Table 5. K-clustering analysis from the fourth principal component analysis dimensions. The cluster numbers are identical to the sample numbers.

Sample	Water potential [kPa]				
	-70	-30	-10	-7	-4
#1	1	1	1	1	24
#2	2	2	2	2	12
#3	3	3	4	4	24
#4	4	4	8	2	11
#5	5	5	5	5	5
#6	6	6	6	6	23

#7	7	7	7	7	20
#8	8	8	6	8	20
#9	9	9	9	9	9
#11	11	18	18	18	18
#12	12	12	12	9	12
#14	14	14	11	11	18
#15	15	11	2	2	2
#18	18	18	18	18	18
#19	19	7	2	2	11
#20	20	20	20	20	20
#21	21	21	9	9	9
#22	22	21	21	21	21
#23	23	23	23	23	23
#24	22	22	22	22	22